Supporting Information

Structure identification and mechanism exploration of ultralow-content of metal-doped Cu for efficient electrochemical production of ammonia in dilute nitrate concentrations

Jiayu Zhan, Lu-Hua Zhang, Yaohua Hong, and Fengshou Yu*

National-Local Joint Engineering Laboratory for Energy Conservation in Chemical Process Integration and Resources Utilization, School of Chemical Engineering and Technology, Hebei University of Technology, Tianjin 300130 (P. R. China)

E-mail: yfsh@hebut.edu.cn (F. Yu)

Experimental Process

Chemicals

Ferric trichloride ($FeCl_3$), sodium hydroxide (NaOH), sodium Nitrate ($NaNO_3$) were purchased from aladdin. Sodium sulfate (Na_2SO_4), sodium dihydrogen phosphate (NaH_2PO_4), disodium hydrogen phosphate (Na_2HPO_4) were purchased from Bide Pharmatech Ltd. Cobalt nitrate hydrate ($Co(NO_3)_2{\cdot}6H_2O$), copper nitrate hydrate ($Cu(NO_3)_2{\cdot}3H_2O$) were purchased from Macklin. Nickel nitrate hydrate ($Ni(NO_3)_2{\cdot}6H_2O$) was purchased from DAMAO. All samples require no further purification before application.

Synthesis of Fe-CuO precursors

The ultra-low content Fe was doped into CuO nanosheet by a simple solvothermal method[1]. Specifically, 4.1 mg $FeCl_3$ was dissolved in 4 mL of anhydrous ethanol, followed by the addition of 1208 mg $Cu(NO_3)_2{\cdot}3H_2O$. Then 40 mL of deionized water at 0 ^oC was added forming a homogeneous solution under stirring. Subsequently, 10 mL of 1.2 M NaOH solution was added by dropping in 1 min and stirred vigorously for 15 min. Then the mixture was transferred into a 100 mL Teflon-lined stainless steel autoclave, and heated at 130 ^oC for 2 h. After cooling to room temperature, the production was collected by diafiltration and washed three times with water and ethanol, then dried under vacuum at 60 ^oC overnight. The Co- and Ni-doped CuO were also obtained by a similar method with Co and Ni precursors, respectively.

Characterization

UV-Vis detection of ion concentrations was carried out with TU-1900. XRD patterns were collected on a JEMARM300F microscope. SEM images were taken on Czech TESCAN MIRA LMS. XPS spectroscopy was performed on a Thermo Scientific ESCALAB 250X. ^1H NMR was used to test the isotope labeling experiments on a BRUKER AVANCE 400.

Electrochemical Testing

The electrochemical investigations were carried out with the CHI760E electrochemical workstation. 4 mg of catalyst was ultrasonically for 5 min with 950 μL of a mixture of ethanol and water (1:1), followed by adding 50 μL of Nafion

solution with 30 min sonication. Then 50 μL of catalyst ink was dropped evenly on the carbon paper and the catalyst loading was 0.2 mg cm^{-2}. The H-type electrolytic cell was adopted for electrocatalytic nitrate reduction reaction (NO_3^-RR). The 1 cm^2 carbon paper (with catalyst) was applied as the working electrode, Ag/AgCl as the reference electrode, and platinum wire as the counter electrode. The obtained Fe-CuO precursors were in-situ reduced to Fe-Cu during the NO_3^-RR process. Post-electrolysis samples were protected by Ar before characterisation.

^{15}N Isotope Labeling Experiments

The isotopic labeling NO_3^-RR experiments were carried out using the aforementioned electrochemical methods with $Na^{15}NO_3$ as N-source. Subsequently, 500 μL of the electrolyte was blended with 200 μL of d^6-DMSO for ^{1}H NMR measurement.

Computation of conversion rate, yield and Faraday efficiency (FE)

The conversion of NO_3^- was computed by Eq. (1):

$$NO_3^- \text{ conversion} = \Delta C_{NO_3^-}/C_0 \times 100\% \quad (1)$$

The yield of NH_4^+ was computed by Eq. (2):

$$\text{Yield}_{NH_4^+} = (C_{NH_4^+} \times V)/(M_{NH_4^+} \times t \times m) \quad (2)$$

The FE was computed by Eq. (3) and (4):

$$FE_{NH_4^+} = (8 \times F \times c \times v)/(M_{NH_4^+} \times Q) \quad (3)$$

$$FE_{NH_4^+} = (2 \times F \times c \times v)/(M_{NH_4^+} \times Q) \quad (4)$$

where $\Delta C_{NO_3^-}$ is the change in NO_3^- concentration before and after electrolysis, C_0 is the onset concentration of NO_3^-, $C_{NH_4^+}$ is the concentration of NH_4^+(aq.), $C_{NO_2^-}$ is the concentration of NO_2^- (aq.), V is the electrolyte volume (30 mL), t is the electrolysis time, m is the mass of catalyst, F is the Faradaic constant (96485 C mol^{-1}), and Q is the total charge passing the electrode.

DFT calculations

The DFT calculations were performed by Vienna Ab initio Simulation Package (VASP)[2, 3] with the projector augmented wave (PAW) method[4]. The generalized gradient approximation (GGA) of Perdew-Burke-Ernzerhof (PBE)[5] functional was applied to treat the exchange-functional. Dispersion forces have been calculated based on Grimme's D3 parameters[6]. The energy cutoff for the plane wave basis expansion was set to 450 eV and the force on each atom less than 0.02 eV/Å was set for convergence criterion of geometry relaxation. The Brillouin zone integration is treated using 3×3×1 k-point sampling. The self-consistent calculations apply a convergence energy threshold of 10^{-5} eV. A 4×4 layer of Cu (111) supercell was built as a model catalyst. To prevent interaction between periodic structures, a vacuum of 20 Å was added along the z direction. We explored the effect of solvation effects on reaction pathways using an implicit solvation model.

The binding strength of different configurations for Fe-Cu catalysts was determined by the binding energy, which is defined as:

$$\Gamma_a = E_{Fe\text{-}Cu} - E_{Cu} - E_{Fe}$$

where $E_{Fe\text{-}Cu}$, E_{Cu}, E_{Fe} are total energies of Fe-doped Cu (111), of Cu (111) slab, and of a single Fe, respectively. In general, the catalyst is thermodynamically more stable when Γ_a is more negative (Table S4). According to DFT calculations, Fe is most stable located at the centre of the Cu surface.

The Gibbs free energy change (ΔG) was used to determine the different adsorption modes and active sites. In general, reaction intermediates are more easily adsorbed with lower ΔG (Table S5).

The binding energy to determine the different adsorption sites of *H on Fe-Cu, which is defined as:

$$\Gamma_b = E_{Fe(H)Cu} - E_{FeCu} - E_H;\ \Gamma = E_{FeCu(H)} - E_{FeCu} - E_H$$

where $E_{Fe(H)Cu}$, $E_{FeCu(H)}$, E_{FeCu}, E_H are total energies of H adsorbed on the Fe atom, on Cu, FeCu slab, and a single H atom, respectively. Our DFT calculations show that *H prefers to adsorb on Fe sites (Table S6).

The free energies of the NO_3^-RR were calculated by the equation: $\Delta G = \Delta E_{DFT} + \Delta E_{ZPE} - T\Delta S$, where ΔE_{DFT} represents the DFT electronic energy difference of every steps. The corrections for zero-point energy (ΔE_{ZPE}) and entropy variation (ΔS) were obtained through VASPKIT. The calculations were performed at a temperature of T = 298.15 K

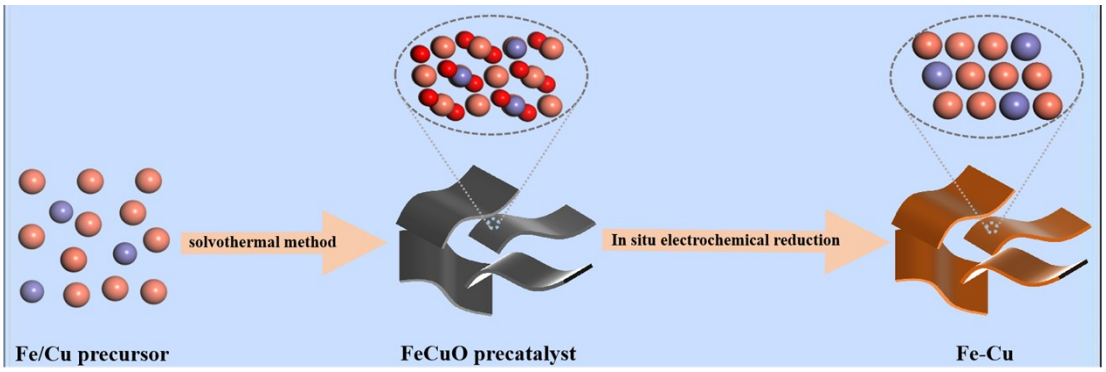

Figure S1. Procedure for Fe-Cu synthesis.

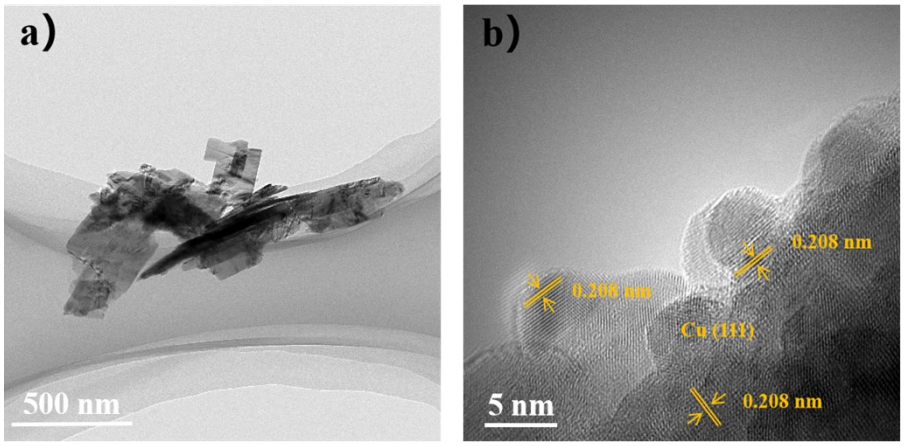

Figure S2. a) TEM and b) high-resolution TEM images of Fe-Cu sample obtained by *in situ* electrochemical reconstitution.

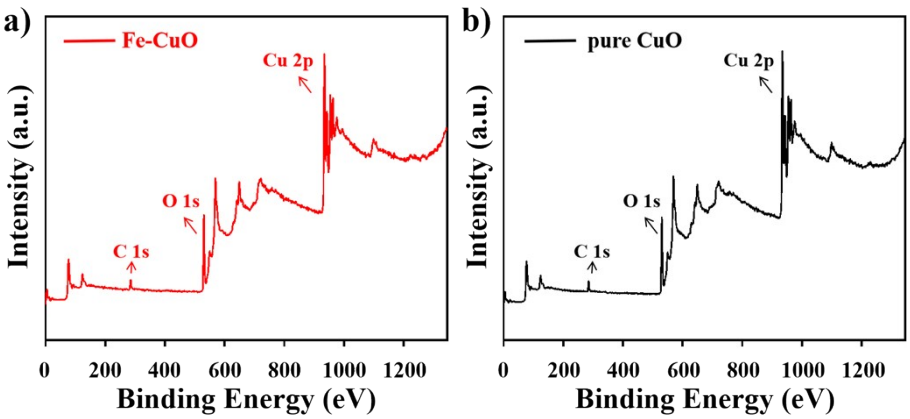

Figure S3. Wide-survey XPS spectra of a) Fe-CuO and b) pure CuO.

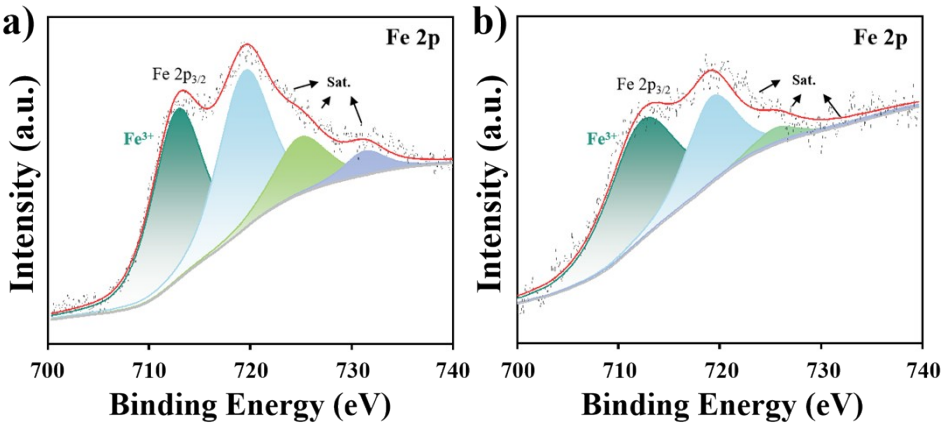

Figure S4. Fe 2p XPS spectra of a) Fe-CuO and b) Fe-Cu.

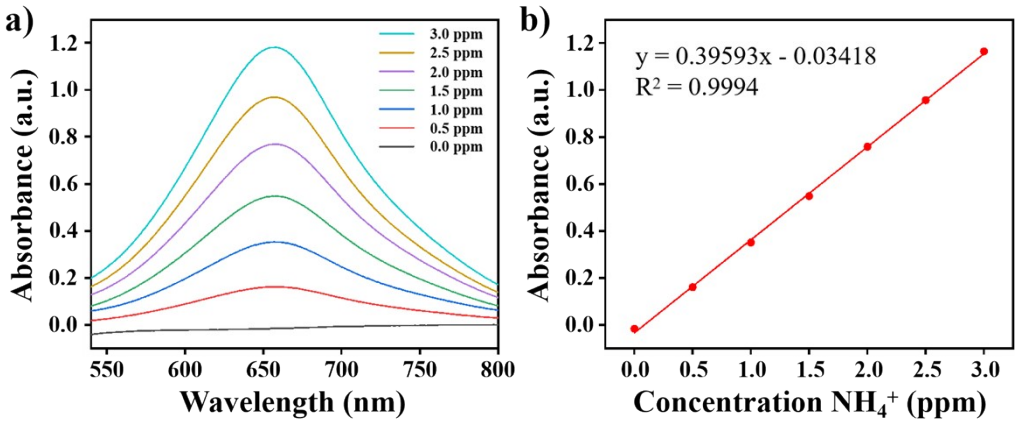

Figure S5. a) Ultraviolet absorption and b) concentration-absorbance calibration curves of NH_4^+.

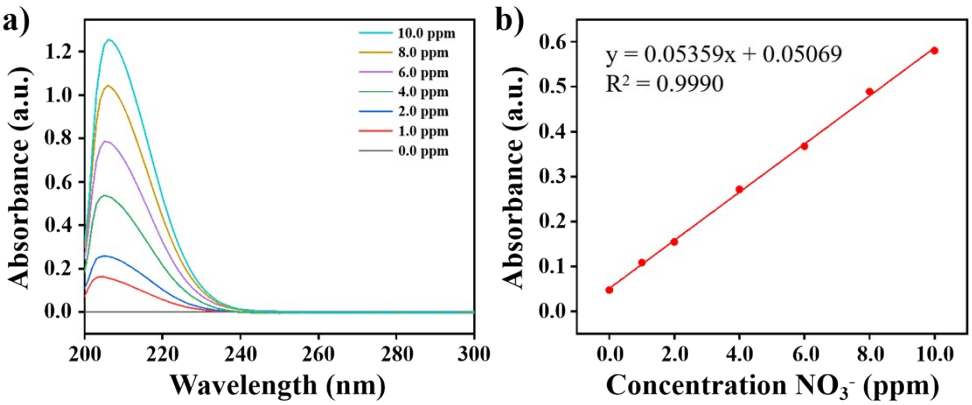

Figure S6. a) Ultraviolet absorption and b) concentration-absorbance calibration curves of NO_3^-.

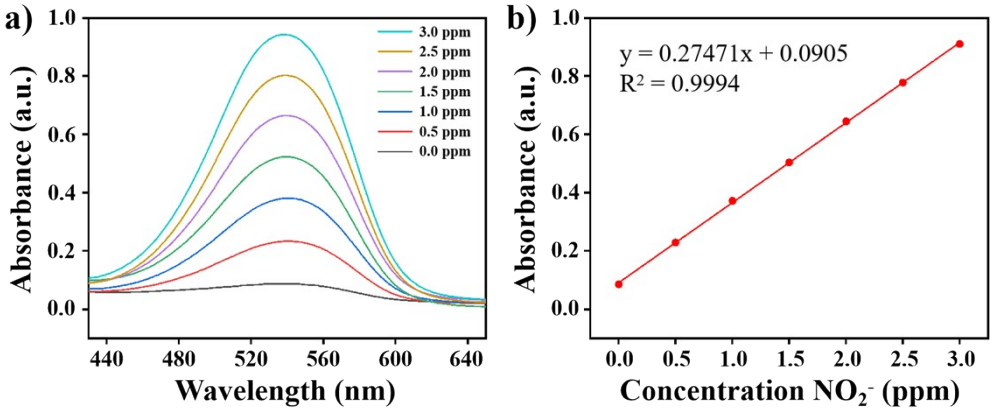

Figure S7. a) Ultraviolet absorption and b) concentration-absorbance calibration curves of NO_2^-.

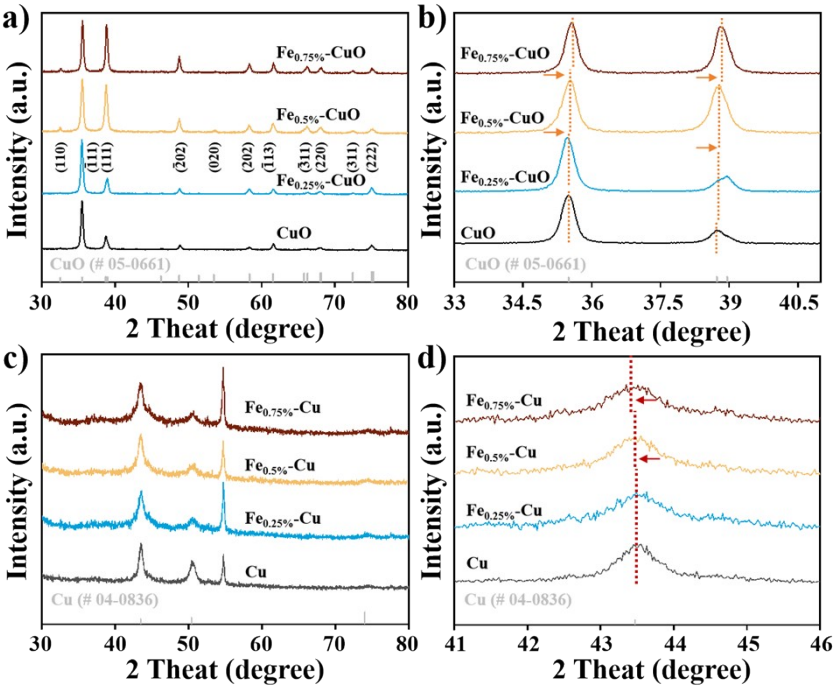

Figure S8. a) XRD patterns and b) the local magnification spectra for $Fe_{0.25\%}$-CuO, $Fe_{0.5\%}$-CuO, $Fe_{0.75\%}$-CuO and CuO; c) XRD pattern and d) local magnification for $Fe_{0.25\%}$-Cu, $Fe_{0.5\%}$-Cu, $Fe_{0.75\%}$-Cu and Cu.

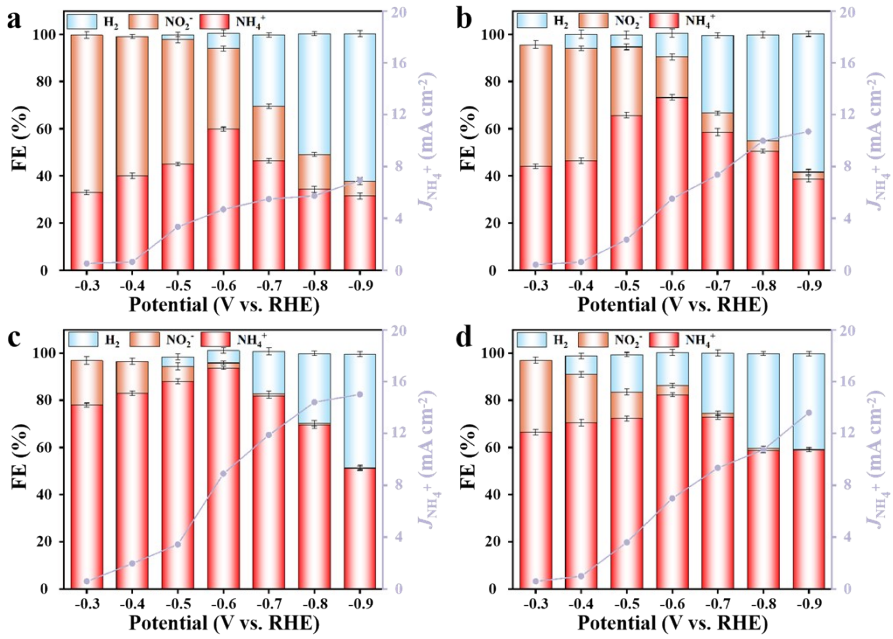

Figure S9. FE of NH_4^+, H_2 and NO_2^- productions with a) Cu, b) $Fe_{0.25\%}$-Cu, c) $Fe_{0.5\%}$-Cu, and d) $Fe_{0.75\%}$-Cu electrodes.

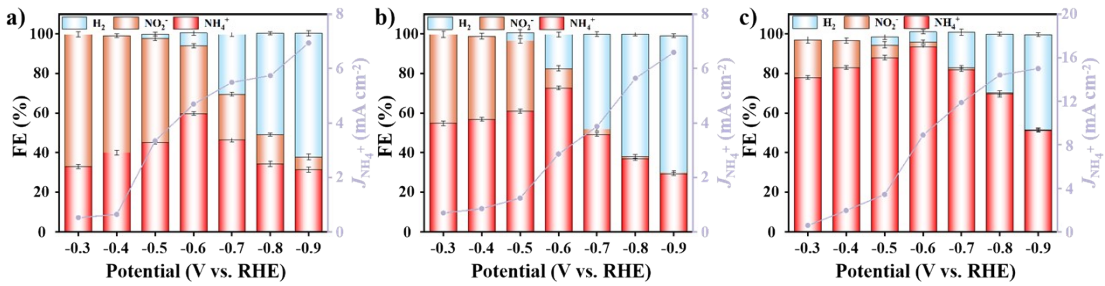

Figure S10. FE of NH_4^+, H_2 and NO_2^- productions with a) Cu, b) Fe/Cu, and c) Fe-Cu electrodes.

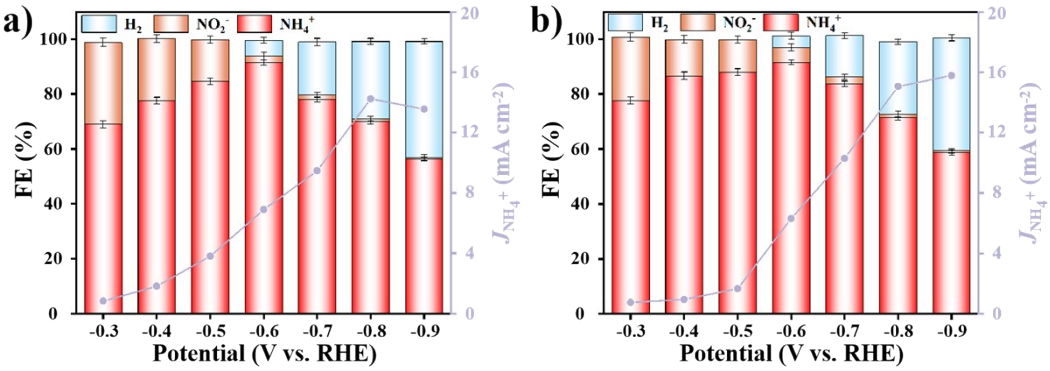

Figure S11. FE of NH_4^+, H_2 and NO_2^- products with a) Co-Cu and b) Ni-Cu.

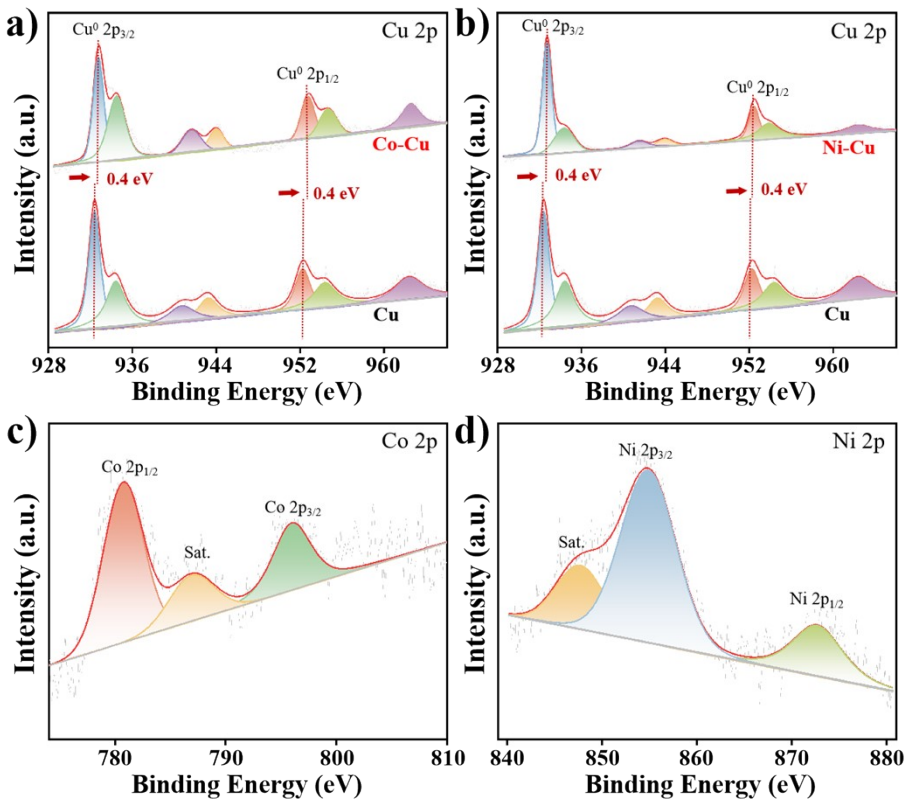

Figure S12. Cu 2p XPS spectra for a) Co-Cu and b) Ni-Cu; c) Co 2p XPS spectra of Co-Cu; d) Ni 2p XPS spectra of Ni-Cu.

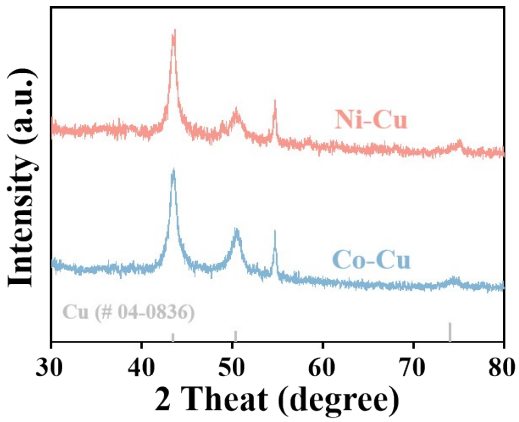

Figure S13. XRD pattern for Co-Cu and Ni-Co.

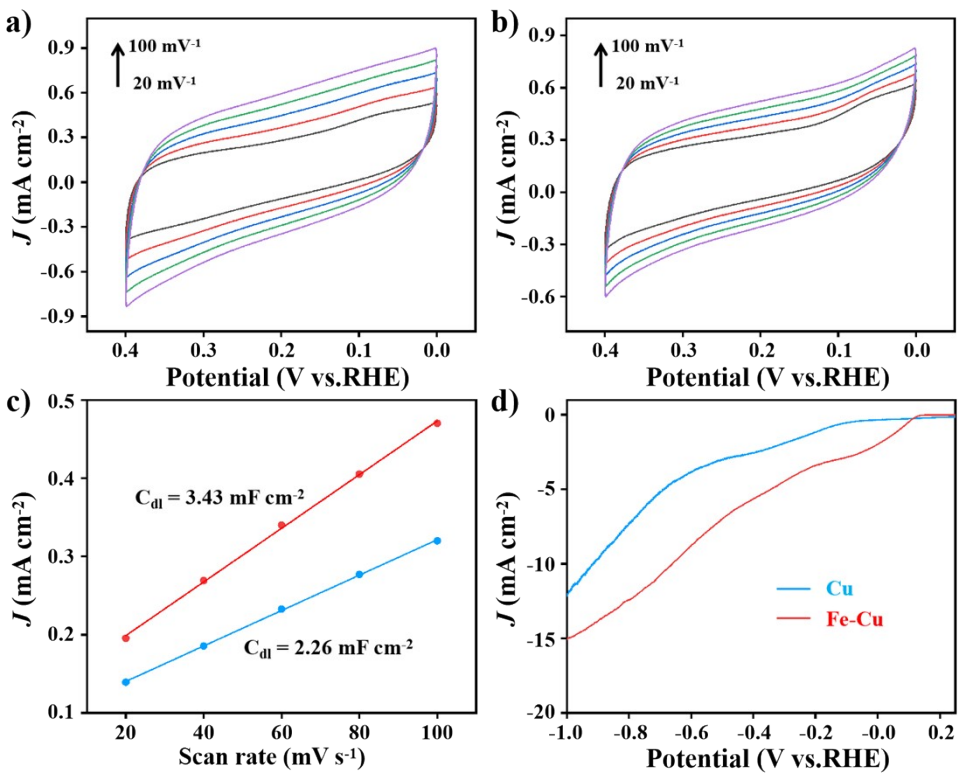

Figure S14. CV curves at various scan rates of a) Cu and b) Fe-Cu; c) the corresponding C_{dl} by ECSA of Cu and Fe-Cu samples; d) ECSA normalized LSV of Cu and Fe-Cu samples.

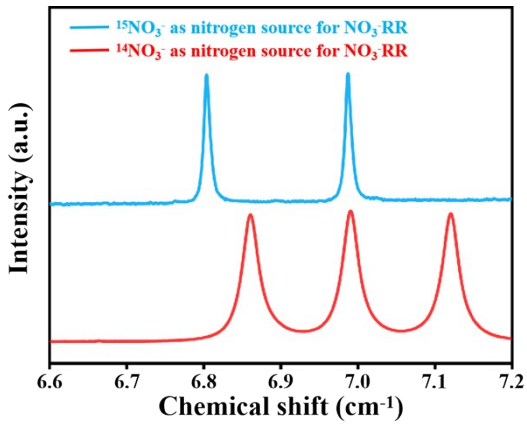

Figure S15. ^{1}H NMR spectra of the electrolyte after the NO_3^- reduction at -0.6 V for 2 h with $Na^{14}NO_3^-$ and $Na^{15}NO_3^-$ as N-source, respectively.

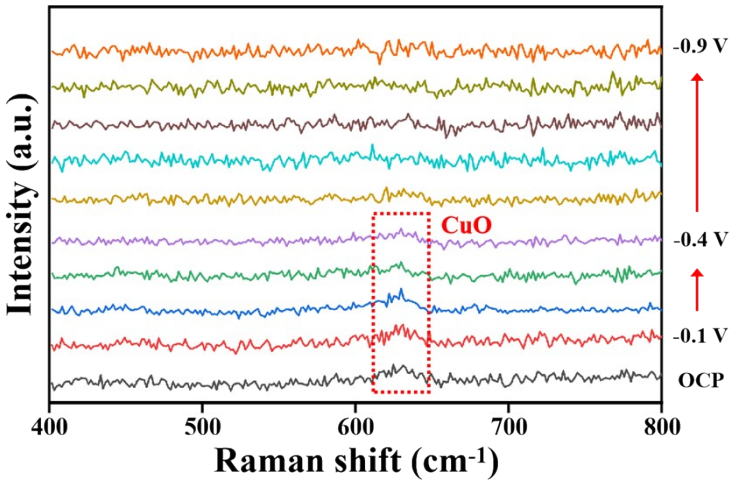

Figure S16. *In situ* Raman spectra for local magnification of Fe-Cu.

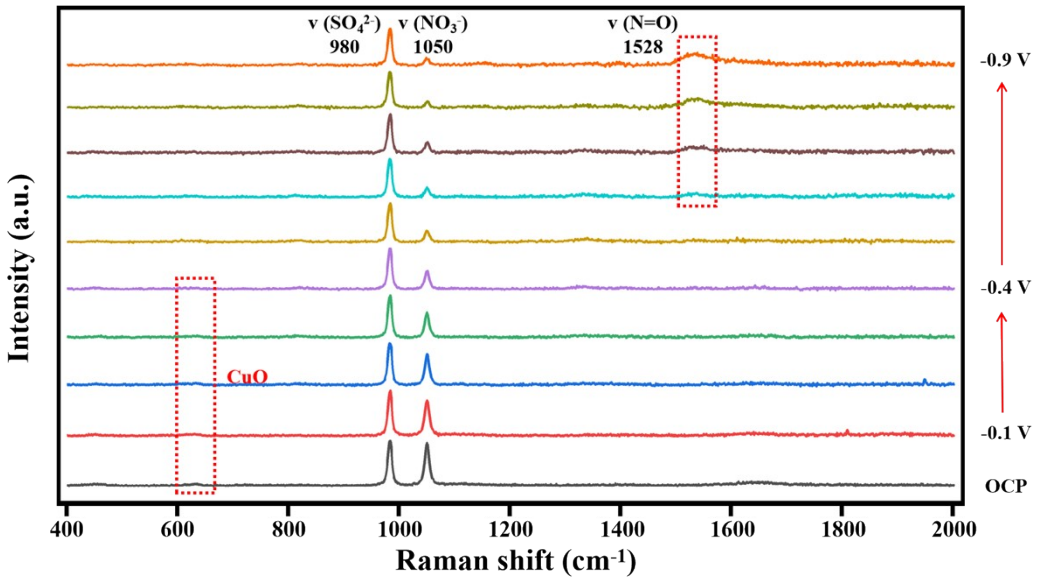

Figure S17. *In situ* Raman spectra of NO_3^-RR with CuO catalyst in 0.5 M Na_2SO_4 and 0.1 M PBS (with 0.1 M NO_3^--N)

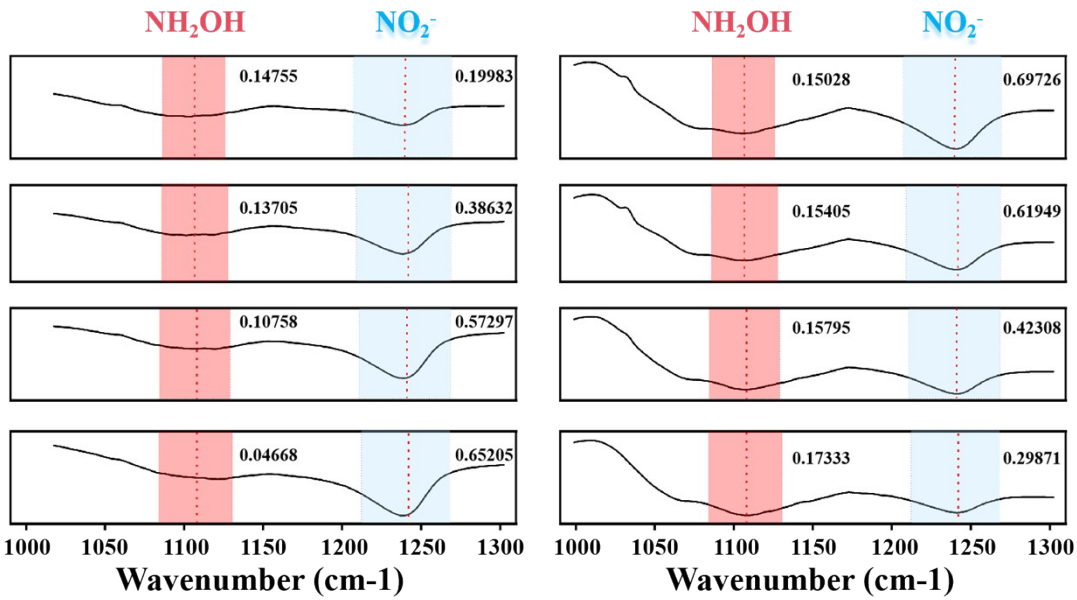

Figure S18. The integration area of NH_2OH and NO_2^- (left Cu and right is Fe-Cu).

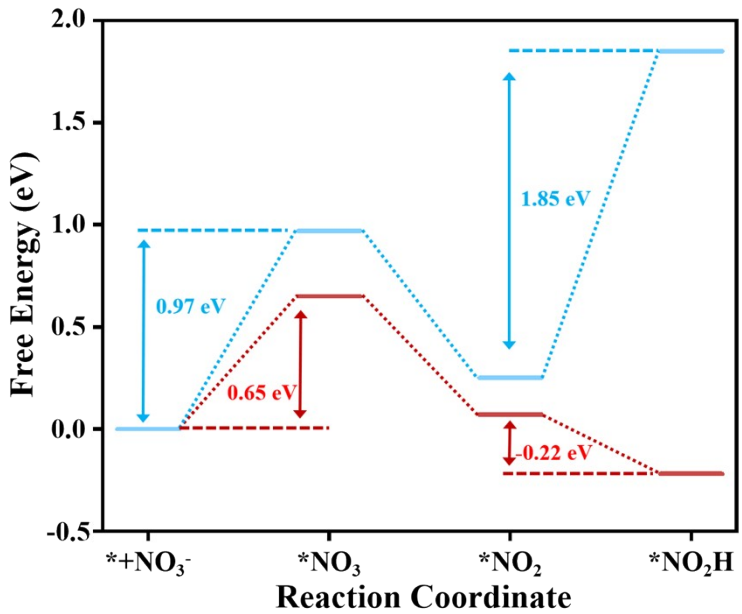

Figure S19. Gibbs free energy diagram of NO_3^- to $*NO_2H$ conversion calculated with the solvation effect

Table S1. The contents of Fe in Fe-CuO and Fe-Cu determined by ICP-MS

Sample	(wt. %)	(at. %)
Fe-CuO	0.26	0.32
Fe-Cu	0.22	0.43

Table S2. The contents of Fe in $Fe_{0.25\%}$-Cu, $Fe_{0.5\%}$-Cu and $Fe_{0.75\%}$-Cu determined by ICP-MS

Sample	(wt. %)	(at. %)
$Fe_{0.25\%}$-Cu	0.10	0.26
$Fe_{0.5\%}$-Cu	0.22	0.43
$Fe_{0.75\%}$-Cu	0.31	0.61

Table S3. Comparison of NH_4^+ yield rate by NO_3^-RR on various catalysts.

Catalysts	Electrolyte	Potential (vs. RHE)	NH_3 yield rate (mmol h^{-1} g_{cat}^{-1})	Ref.
Fe-Cu	**100 ppm NO_3^--N, 0.5 M Na_2SO_4**	**-0.9 V**	**323.1**	**This work**
CuCl_BEF	100 ppm NO_3^--N, 0.5 M Na_2SO_4	-1.0 V	97.3	[7]
CuPc@Mxene	50 ppm NO_3^--N, 0.5 M Na_2SO_4	-1.06 V	84.7	[8]
Plasma treated Cu_2O	50 ppm NO_3^--N, 0.5 M Na_2SO_4	-0.58 V	83.0	[9]
Pd-Cu_2O CEO	50 ppm NO_3^--N, 0.5 M Na_2SO_4	-1.3 V	54.4	[10]
TiO_{2-X}	50 ppm NO_3^--N, 0.5 M Na_2SO_4	-0.74 V	45.0	[11]
10Cu/TiO_{2-X}	200 ppm NO_3^--N, 0.5 M Na_2SO_4	-0.75 V	114.3	[12]

Table S4. Binding energies (Γ) of Fe doping at different sites of Cu (111).

	On Surface		
	Centre	Edge	Corner
Γ (kJ/mol)	-301	-289	-298
Structure	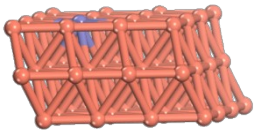	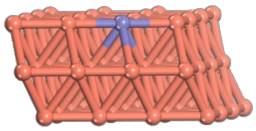	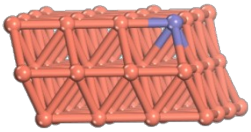
	On Subsurface		

	First Subsurface Layer	Second Subsurface Layer
Γ (kJ/mol)	-276	-269
Structure	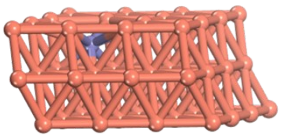	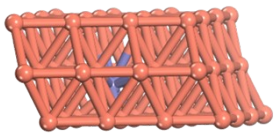

Table S5. Dependence of ΔG for NO_3^- adsorption on the adsorption site and the corresponding structure.

Adsorption sites	Bridge adsorption	
	Cu	Cu and Fe
Δ G (eV)	0.79	0.85
Structure	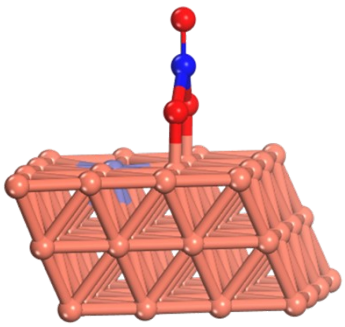	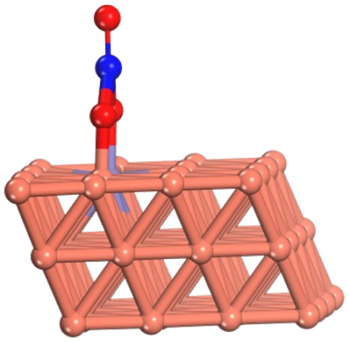
Adsorption sites	top adsorption	
	Cu	Fe
Δ G (eV)	1.22	1.38
Structure	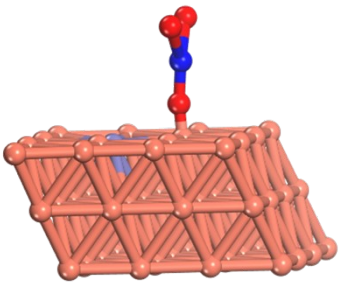	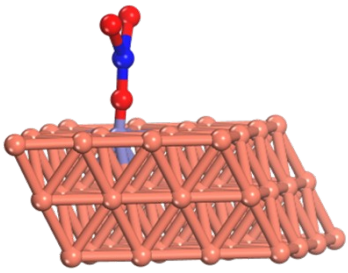

Table S6. Binding energies (Γ) of *H at different sites of Fe and Cu.

	*H occupies the Fe	*H occupies the Cu
Γ (kJ/mol)	-353	-344

Structure	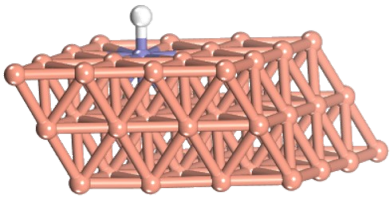	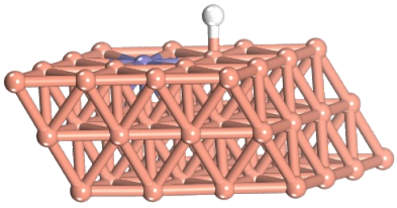

References

1. W. Li, L. Li, Q. Xia, S. Hong, L. Wang, Z. Yao, T.-S. Wu, Y.-L. Soo, H. Zhang, T. W. B. Lo, A. W. Robertson, Q. Liu, L. Hao and Z. Sun, *Appl. Catal. B Environ.*, 2022, **318**.
2. K. Ohkawa, K. Hashimoto, A. Fujishima, Y. Noguchi and S. Nakayama, *J Electroanal. Chem*., 1993, **345**, 445-456.
3. J. Hafner, *J Comput. Chem.*, 2008, **29**, 2044-2078.
4. G.Kresse and J.Furthmüller, *J Phys. Rev. B*, 1996, **54**,11169.
5. P. E. Blochl, *Phys. Rev. B*, 1994, **50**, 17953-17979.
6. S. Grimme, J. Antony, S. Ehrlich and H. Krieg, *J. Chem. Phys.*, 2010, **132**.
7. W. J. Sun, H. Q. Ji, L. X. Li, H. Y. Zhang, Z. K. Wang, J. H. He and J. M. Lu, *Angew. Chem. Int. Ed.*, 2021, **60**, 22933-22939.
8. L.-X. Li, W.-J. Sun, H.-Y. Zhang, J.-L. Wei, S.-X. Wang, J.-H. He, N.-J. Li, Q.-F. Xu, D.-Y. Chen, H. Li and J.-M. Lu, *J. Materials. Chem. A*, 2021, **9**, 21771-21778.
9. Z. Gong, W. Zhong, Z. He, Q. Liu, H. Chen, D. Zhou, N. Zhang, X. Kang and Y. Chen, *Appl. Catal. B Environ.*, 2022, **305**.
10. Y. Xu, K. Ren, T. Ren, M. Wang, Z. Wang, X. Li, L. Wang and H. Wang, *Appl. Catal. B Environ.*, 2022, **306**.
11. R. Jia, Y. Wang, C. Wang, Y. Ling, Y. Yu and B. Zhang, *ACS Catal.*, 2020, **10**, 3533-3540.
12. X. Zhang, C. Wang, Y. Guo, B. Zhang, Y. Wang and Y. Yu, *Journal of Materials Chemistry A*, 2022, **10**, 6448-6453.